

Electron Microscopy Observation of TiO₂ Nanocrystal Evolution in High-Temperature Atomic Layer Deposition

Jian Shi,^{†,⊥} Zhaodong Li,[†] Alexander Kvit,^{†,‡} Sergiy Krylyuk,^{§,||} Albert V. Davydov,[§] and Xudong Wang^{*,†}

[†]Department of Materials Science and Engineering and [‡]Materials Science Center, University of Wisconsin-Madison, Madison, Wisconsin 53706, United States

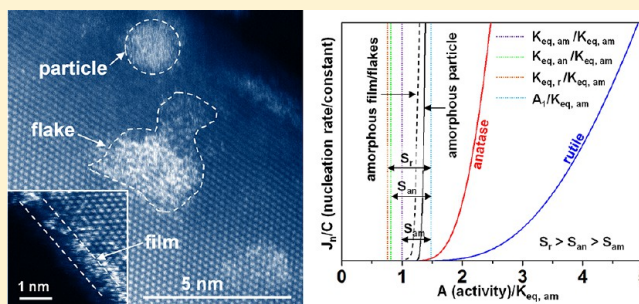
[§]Material Measurement Laboratory, National Institute of Standards and Technology, Gaithersburg, Maryland 20899, United States

^{||}Institute for Research in Electronics and Applied Physics, University of Maryland, College Park, Maryland 20742, United States

S Supporting Information

ABSTRACT: Understanding the evolution of amorphous and crystalline phases during atomic layer deposition (ALD) is essential for creating high quality dielectrics, multifunctional films/coatings, and predictable surface functionalization. Through comprehensive atomistic electron microscopy study of ALD TiO₂ nanostructures at designed growth cycles, we revealed the transformation process and sequence of atom arrangement during TiO₂ ALD growth. Evolution of TiO₂ nanostructures in ALD was found following a path from amorphous layers to amorphous particles to metastable crystallites and ultimately to stable crystalline forms. Such a phase evolution is a manifestation of the Ostwald–Lussac Law, which governs the advent sequence and amount ratio of different phases in high-temperature TiO₂ ALD nanostructures. The amorphous–crystalline mixture also enables a unique anisotropic crystal growth behavior at high temperature forming TiO₂ nanorods via the principle of vapor-phase oriented attachment.

KEYWORDS: TiO₂, atomic layer deposition, Ostwald–Lussac law, oriented attachment



Atomic layer deposition (ALD) is a unique thin film growth technique based on sequential self-limiting surface reactions.¹ It offers high quality, pinhole-free, and conformal thin films with precise thickness control down to subnanometers.² During the past decades, it has demonstrated significant advancements in growing gate dielectrics in complementary metal oxide semiconductor (CMOS) devices, insulating layers in memory devices, optical coating in photonic devices, and surface modification/functionalization for catalysts.^{3–7} Many research efforts have been devoted to explore the roughness control, surface chemical properties, and conformal coating features of ALD films, which are either amorphous or crystalline.^{2,8,9} Contemporary research on ALD extends to exploring continuous and rapid film growth at ambient pressure and conformally depositing quantum dots, nanowires (NWs), or epitaxial films.^{10–19} Such novel advances would make ALD a powerful and versatile nanomanufacturing tool beyond a thin film coating technique. Nevertheless, current understanding of ALD growth is mainly based on surface chemistry, that is, molecular level chemical reactions.⁸ Although this general understanding can be adequately applied to amorphous thin film deposition at low temperature, it often meets obstacles when interpreting surface roughness, morphology, crystallinity, and physical properties.^{15,16} Therefore, obtaining atomic-level understanding of the phase evolution in ALD is critical for achieving morphology, crystal structure,

and property control, as well as deposition manipulation and scaling.

Recently, our research revealed that by raising the deposition temperature to 600 °C, growth kinetics of TiO₂ ALD was modified and yielded anisotropic one-dimensional (1D) crystal growth instead of forming 2D polycrystalline films (this process was also named surface reaction-limited pulsed chemical vapor deposition, or SPCVD).¹⁴ As a result, nanorod (NR) arrays were uniformly deposited inside highly confined submicrometer-sized spaces, such as inside anodized alumina oxide (AAO) nanochannels and among dense and deep Si NW forests, offering a novel hierarchical NW architecture with enhanced electrical and electrochemical properties.^{14,15} This unique growth behavior does not follow the conventional growth models of polycrystalline or epitaxial oxides via ALD. It thus provides a valuable platform for studying and comparing phase evolution during ALD process. In this report, we present a comprehensive atomistic study of crystal nucleation and growth behaviors of TiO₂ nanostructures grown by ALD. By applying aberration-corrected scanning transmission electron microscopy (STEM) and TEM characterization, we revealed the transformation process and sequence of atom arrangement during high-temperature TiO₂ ALD growth, where the

Received: September 24, 2013

Published: October 4, 2013

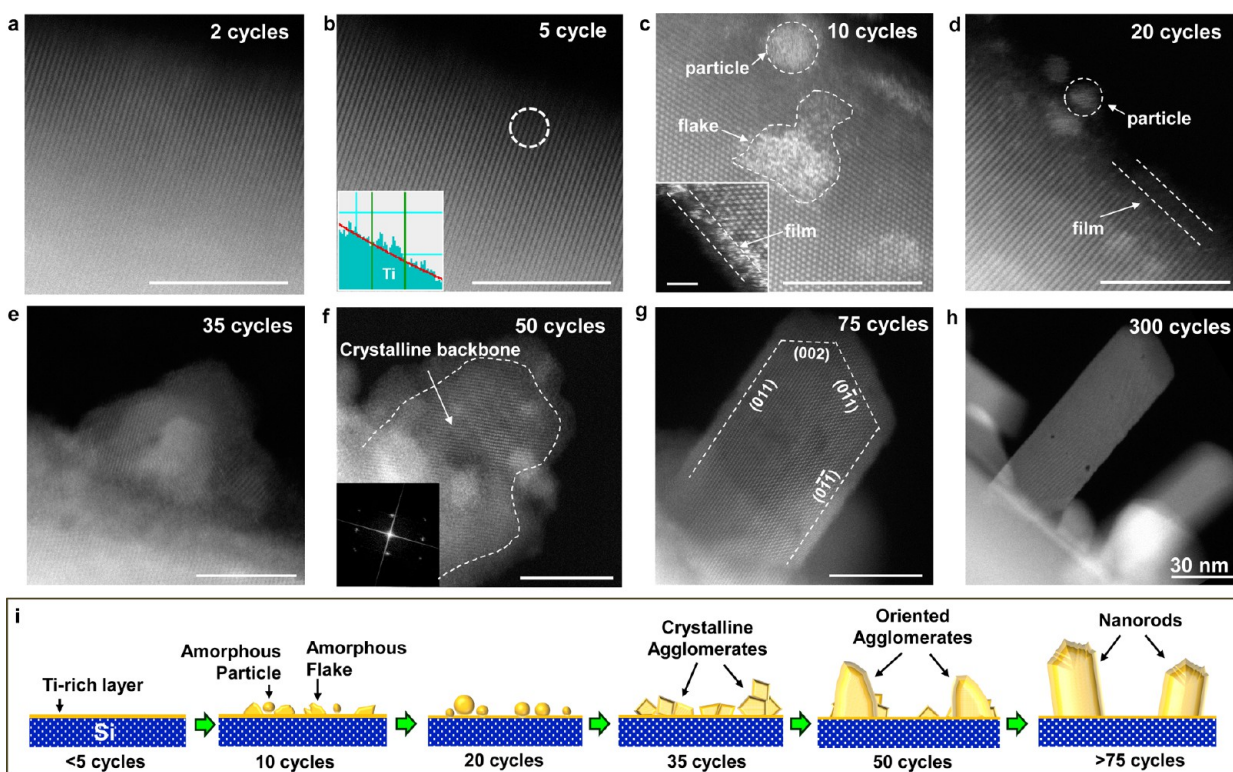


Figure 1. Evolution of TiO_2 NRs at different ALD cycles at 600°C revealed by HR HAADF STEM. (a) Two cycle and (b), 5 cycle growth did not show noticeable TiO_x morphology on a single crystalline Si NW, while EELS analysis (inset of b) on 5 cycle sample detected the existence of Ti on the Si NW edge. (c) Ten cycle growth: TiO_x nanoparticles and flakes were observed on the Si NW surfaces. Inset shows the amorphous ultrathin TiO_x layer coated on NW substrate (scale bar is 1 nm). (d) Twenty cycle growth: TiO_x flakes disappeared while particles and films still existed. (e) Thirty-five cycle growth: majority of TiO_x morphology was found to be the agglomeration of amorphous layer-coated TiO_2 crystallites. (f) Fifty cycle growth: TiO_2 NR embryo was formed by the self-organization and alignment of individual TiO_2 crystallites. Inset is the corresponding FFT pattern converted from lattice image. (g) Seventy-five cycle growth: early stage TiO_2 NR was evolved with well-defined side walls and canonical growth front. (h) Three hundred cycle growth: ultimate TiO_2 NR morphology was formed with two anatase (011) and two (100) as sides facets and one (0 $\bar{1}$ 1) and one (002) as growth front facets. (i) Schematic illustration of the entire evolution process of TiO_2 NRs. Scale bars are 5 nm unless otherwise noted.

Ostwald–Lussac law^{20–22} was found to be the governing rule of phase evolution. This discovery provides a new understanding of morphology and crystal evolution during ALD of crystalline nanostructures. At high temperature, the amorphous–crystalline ALD mixture can enable a unique anisotropic crystal growth behavior forming TiO_2 nanorods via the principle of vapor-phase oriented attachment.

Crystal evolution was first investigated from TiO_2 nanostructures deposited at 600°C (the conditions favoring NR formation). Detailed experimental information can be found in the Supporting Information. In order to obtain sharp interface and high-quality STEM images, single-crystalline ZnO and Si NWs were used as supporting surfaces. Figure 1 shows a series of high-resolution high-angle annular dark-field STEM (HR HAADF STEM) images taken at the interfaces between TiO_2 and supporting Si NWs, where different growth stages are indexed by the ALD growth cycles. Corresponding low-magnification STEM images can be found in Supporting Information, Figure S1. At the beginning of growth (1–5 cycles), there are no noticeable TiO_2 morphologies such as films or islands (Figure 1a,b); while electron energy loss spectroscopy (EELS) analysis reveals the existence of Ti elements from the Si NW edge. This is known as the initiation stage, where the deposition is controlled by reaction between precursor molecules and surface active bonds and exhibits the lowest growth rate.⁸ At 10 cycles, three typical morphologies

emerged as shown in Figure 1c: cloudy and loosen amorphous flakes with diameters ranging from 1 to 2 nm; ultrathin amorphous film covering the surface of Si NW with a thickness of several angstroms (inset of Figure 1c); and sparsely distributed fuzzy amorphous particles with a diameter of ~ 1 nm. When growth proceeds to 20 cycles, amorphous particles and ultrathin films became the dominating morphologies (Figure 1d). The density of amorphous particles at the 20-cycle stage largely increased compared to the 10-cycle samples, while similar diameters remained. In addition, no cloudy flakes were observed at this stage suggesting that the flakes are unstable transient morphology. After 35 cycles of growth, the NW surfaces were covered with larger nanoparticles (5–10 nm), which were agglomeration of small crystallites shelled by thin amorphous layers (Figure 1e and Supporting Information Figure S2). The amorphous layer surrounding the crystalline agglomeration is believed to be a fingerprint of ALD prior to phase transformation. As the growth proceeded to 50 cycles, the integrated nanoparticle assemblage became larger and its elongated shape appeared like embryos of NRs (~ 10 nm wide and ~ 20 nm long, Figure 1f). Both HR HAADF STEM image and its fast Fourier transform (FFT) (right inset of Figure 1f) show that most small crystallites in the nanoparticle assemblage had the same orientation. A thin amorphous layer was also observed in the outmost region of the bulk embryos. At 75 cycles, high-density miniature NR-like single crystals of ~ 20 nm

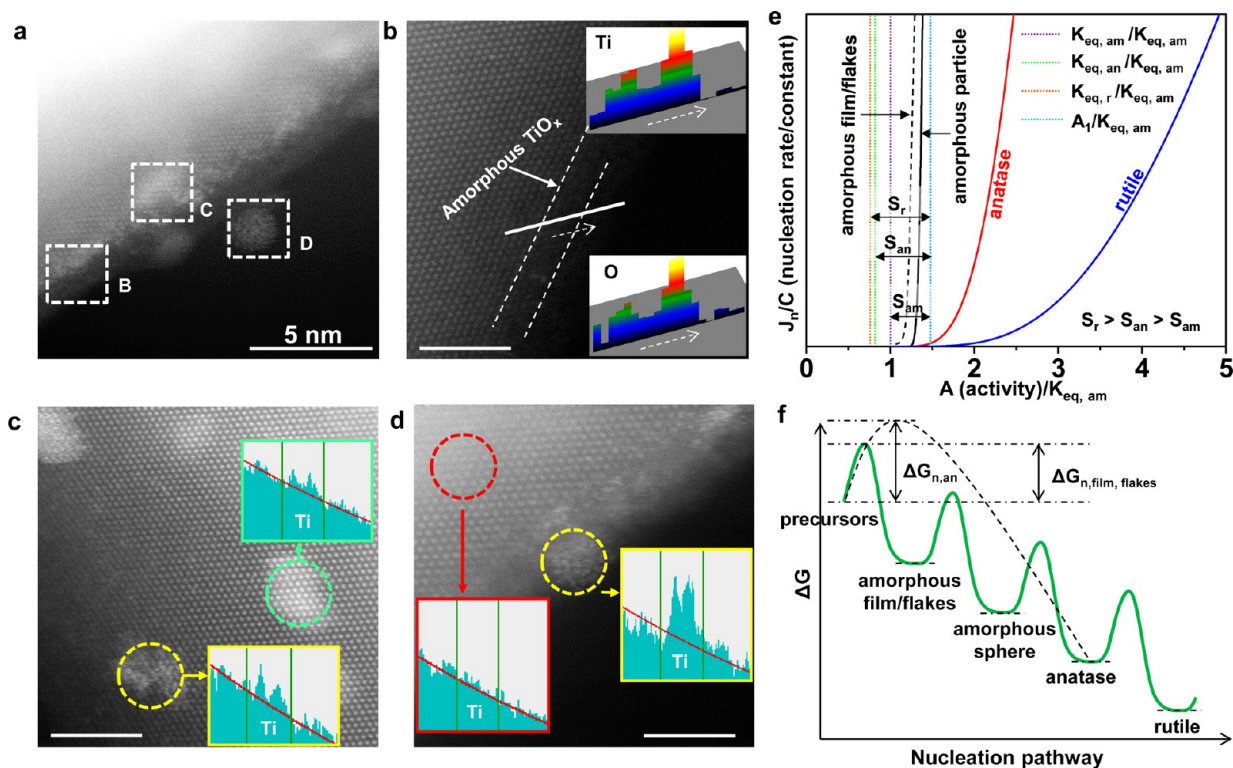


Figure 2. Direct observation of Ostwald–Lussac Law at 600 °C ALD growth. (a) Three typical TiO₂ morphologies were observed to coexist from 10-cycle ALD sample. (b) An ultrathin amorphous TiO_x layer with subnanometer thickness on Si NW after 10 cycles ALD growth. Insets show the Ti and O EELS profiles (lighter color indicates stronger signals) along the indexed direction on the NW edge. (c) The flake morphology sparsely distributed on Si NW surface. Insets are EELS spectra showing the flakes have concentrated Ti. (d) The particle morphology (yellow circle) have much stronger Ti signal than flakes, while no sensible Ti signal was found from the bare NW surface. (e) Nucleation rate of different phases of TiO₂ versus the precursor's activity product. K_{eq} represents the equilibrium products, natural logarithms of S are defined as the supersaturations under the fixed activity A_1 ($\ln S = A_1/K_{eq}$). Subscripts am, an, and r stand for amorphous, anatase, and rutile phases of TiO₂, respectively. (f) Schematic energy landscape of a series of TiO₂ phases illustrating the nucleation pathway. At certain degree of supersaturation, crystal growth tends to proceed along its adjacent crystal phases step by step toward anatase phase because the nucleation barrier of anatase TiO₂ ($\Delta G_{n,an}$) is higher than its adjacent phases ($\Delta G_{n, film/flake}$). Scale bars are 2 nm unless otherwise noted.

wide and ~40 nm long started to form (Figure 1g). Eventually, typical high-aspect ratio TiO₂ NRs (width, ~40 nm; length, ~200 nm) were received after longer growth cycles (Figure 1h and Supporting Information Figures S3 and S4). The entire NR evolution process is schematically shown in Figure 1i.

HR HAADF STEM observation suggests that the formation of TiO₂ NRs at 600 °C consists of two processes: evolution of crystallites from amorphous nanoparticles via phase transformation; and self-organization of the crystallites into polycrystalline nanoparticles assemblage. These two processes were confirmed by high-resolution transmission electron microscopy (HRTEM) (Supporting Information Figure S5), where the amorphous layer wrapping around the emerging crystallites can be clearly observed. To further confirm this self-organization process, a 25-cycle ALD amorphous TiO_x film grown on silicon nitride membrane was illuminated under electron-beam in the TEM chamber (the beam current and duration conditions were optimized to reduce sample damage), while its crystal structure evolution was continuously monitored. In situ HRTEM imaging shows that the emerging crystallites first formed a chain with aligned orientations and then grew outward by attaching more crystallites (Supporting Information Figure S6). This self-organization process, known as oriented attachment growth, was originally discovered in hydrothermal growth of TiO₂ NWs and later was found to be a generic solution-based growth mechanism in a variety of

crystals.^{23,24} To our best knowledge, this is the first observation of oriented attachment growth in vapor-solid process, which may be a result of high surface hydroxyl group density from extended H₂O pulses.

Observation of the metastable phases and percolated films at high temperature is not accordant with the general understanding of ALD film growth and crystallization, which states that a crystalline film often starts with crystal nuclei followed by the self-limited layer-by-layer crystal growth.^{18,25} In order to clearly illustrate such a unique nucleation process, atomic-scale elemental analysis was performed along the surface of a 10-cycle product, where the three typical transitional morphologies (film, flake, and particle) coexist (Figure 2a). From EELS collected over the three morphologies (Figure 2b–d), distinct Ti signals were identified on each of them (TiL3 at 458 eV and TiL2 at 463 eV).²⁶ Surface amorphous film (Figure 2b) and cloudy loosen flakes (Figure 2c) are the two first appearing nuclei forms. EELS spectra indicate that the density of Ti in such film/flake structures is much lower than that in the amorphous particles. The sparse amorphous nanoparticles are believed to be more stable nuclei form that were transformed from the flakes since a larger quantity of such particles was observed at longer growth cycles with the consumption of flakes (Figure 2d). At 25 cycles, crystalline phase (identified to be anatase) started to emerge inside amorphous particles. X-ray diffraction spectra (XRD) show that the anatase phase persisted

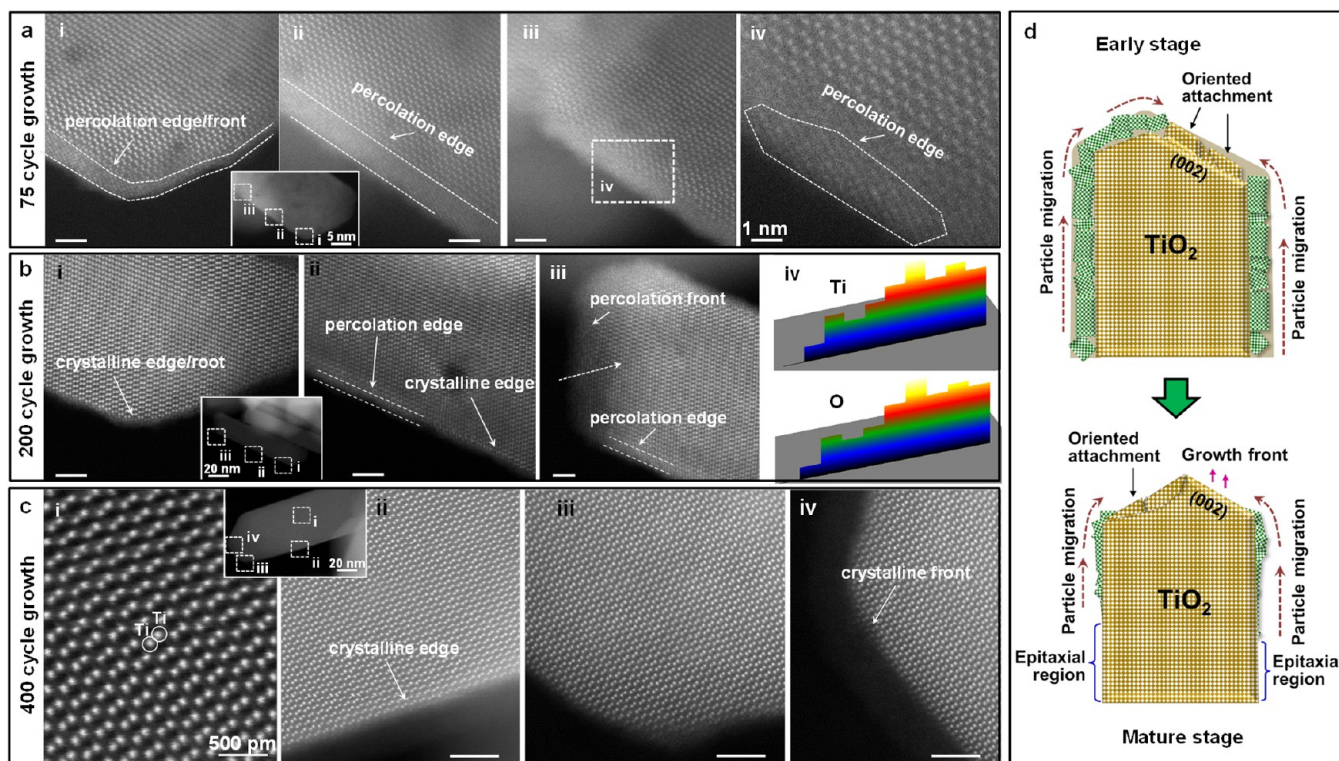


Figure 3. Vapor phase oriented attachment growth of TiO₂ NR by 600 °C ALD. (a) Atomic structure of NR grown at 75 cycles. Its tip (i), middle (ii), and root (iii) regions all have a 1–2 nm thick amorphous/crystalline percolated film, which is highlighted by the magnified root region (iv). (b) Atomic structure of NR grown at 200 cycles. (i) Well-defined (002) and (011) facets composing the NR root were found to be percolated film-free. (ii) A transient region with atomically flat (011) surface near the root of NR and percolated film-coated (011) surface near the tip region. (iii) The fuzzy NR tip with thicker percolated film. (iv) EELS line scan profiles show the growth front was much thinner in its outmost tip region while thicker close to its body. (c) Atomic structure of NR grown at 400 cycles. Its body (i), middle (ii), front (iii), and tip (iv) regions all exhibited high-quality crystal structure and are percolated film-free. No dislocation or stacking faults were spotted. The thick amorphous layer shown in (iv) is a result of carbon deposition during long-time imaging. (d) Schematics showing the oriented attachment process that is responsible for the anisotropic growth of a TiO₂ NR. Scale bars are 2 nm unless otherwise noted.

until the growth reached 900 cycles, where a slight amount of rutile structure started to appear (Supporting Information Figure S7). Therefore, the entire TiO₂ crystal evolution pathway at high-temperature (high-T) can be summarized as: amorphous film/flakes → amorphous particles → anatase → rutile.

Thermodynamic data from literature shows that $-\Delta G_{f, \text{rutile}} > -\Delta G_{f, \text{anatase}} > -\Delta G_{f, \text{amorphous}}$.^{27,28} It has also been reported that the stability of such cloudy and loosen structures is generally much lower than a dense or crystalline phase in many crystal systems.^{29,30} Thus, simple thermodynamic theory is not sufficient to explain the TiO₂ crystal evolution observed at 600 °C via ALD. The formation of transient metastable TiO₂ phases during the nucleation pathway in fact follows the empirical Ostwald–Lussac Law. This law states that an unstable system does not necessarily transform directly into the most stable phase but likely into one that most closely resembles itself.^{20,21} In terms of energy, the phase transformation is always accompanied by the minimum energy loss. Such a non-equilibrium process therefore involves more kinetic concepts. To further prove the observed high-T TiO₂ crystal evolution is a case of Ostwald–Lussac Law, the nucleation process under 600 °C ALD was quantitatively modeled.

For any kinetically limited chemical process, the nucleation probability is proportional to the exponential of the barrier height divided by $k_B T$, where k_B is Boltzmann constant, and T is the nucleation temperature. The nucleation rate is given by³¹

$$J_n = A \exp\left(-\frac{\Delta g_n}{k_B T}\right) \quad (1)$$

where A is a constant factor. SI units are used for all terms units unless otherwise noted. The nucleation barrier can be substituted by surface free energy and supersaturation [$\ln S$ (supersaturation) = AP (activity product)/ K (equilibrium product)]. The supersaturation here deals with the chemically absorbed precursor molecules. In the case of high-temperature TiO₂ deposition, the active surface dangling bonds are considered movable and can be regenerated due to HCl side reactions.³² Therefore, the chemically absorbed molecules could diffuse on the crystal or substrate surfaces, and form clusters and then nuclei for nanorod growth. The activity product is thus defined as that “activity of one gas-phase specie (water or TiCl₄)” times “activity of available dangling bonds on substrates (Ti–Cl or O–H)”. Thus, the final form of nucleation rate can therefore be presented as (detailed derivation is given in S7),

$$J_n = A \exp\left(-B \frac{\gamma^3}{(\ln S)^2}\right) \quad (2)$$

where γ is the surface free energy of nucleus. Equation 2 suggests that the nucleation rate is strongly dependent on the second power of supersaturation and third power of surface free energy. Figure 2e shows the nucleation rates of amorphous

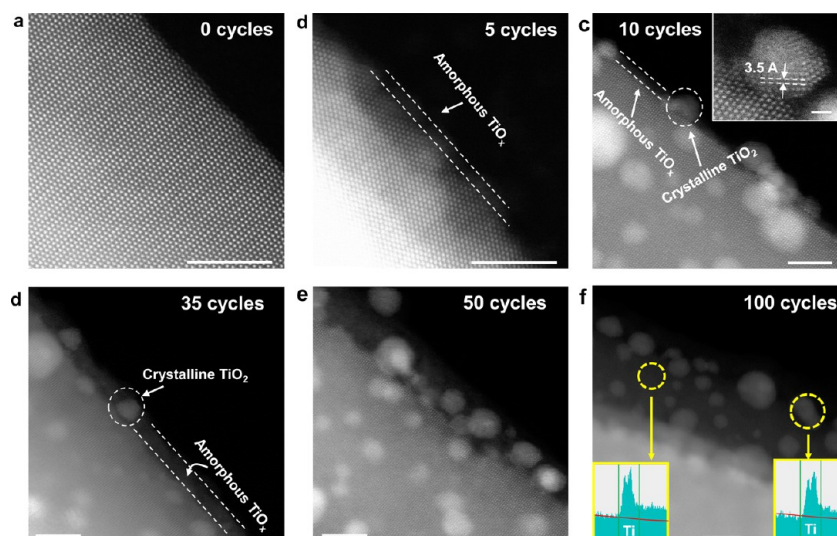


Figure 4. ALD growth of TiO₂ film on ZnO NW at 300 °C. (a) A STEM image of a bare ZnO NW prior to ALD growth. (b) Five cycle growth: small amorphous TiO₂ islands start to form on ZnO NW. (c) Ten cycle growth: crystalline TiO₂ particles appeared with a thin but uniform and continuous amorphous TiO₂ film covering the ZnO NW surface. Inset shows the crystallinity of a 2 nm TiO₂ particle (scale bar is 1 nm). (d) Thirty-five cycle growth: both TiO₂ crystalline particles and amorphous films grew larger and thicker. (e) Fifty cycle growth: TiO₂ crystalline particles continued to grow larger and became buried by the thicker TiO₂ film. (f) One Hundred cycle growth: amorphous TiO₂ film reached ~10 nm thick and various sized crystalline TiO₂ particles were observed. The EELS analysis demonstrates that both amorphous and crystalline phases have similar amounts of Ti and Ti/O ratio. Scale bars are 5 nm unless otherwise noted.

film/flakes, amorphous particles, anatase, and rutile phases of TiO₂ versus activity product of the precursors divided by the equilibrium product of amorphous particles. Solid lines are plotted based on above formulas and the dashed black line is deduced from our experimental observation. The color dash lines are applied to qualitatively illustrate the normalized equilibrium products of amorphous nanoparticles, anatase and rutile structures and the precursor activity. According to Figure 2e, though the supersaturation of anatase TiO₂ is higher than amorphous nanoparticles at any randomly chosen considerable activity product ($\ln S_{\text{anatase}} > \ln S_{\text{amorphous particle}}$), its nucleation rate is much lower than the amorphous nanoparticles. This perfectly agrees with our discovery from the 600 °C ALD results. The key factor yielding such a nucleation pathway is the drastic difference of surface free energies among different phases of TiO₂, which has more influence (3rd power) on the nucleation rates following eq 2: a smaller surface free energy yields a much higher nucleation rate. Atomic structure of disordered phase is closer to vapor precursors compared to well-crystallized ones, and thus possesses smaller surface free energy difference from vapor phase.³³ Literature reports revealed that the surface free energies of the three phases in Figure 2e follow the relation: $\gamma_{\text{amorphous particles}} < \gamma_{\text{anatase}} < \gamma_{\text{rutile}}$.^{27,34,35} Therefore, the energy landscape of nucleation pathway from reaction precursors to final rutile phase is schematically illustrated in Figure 2f. Although Gibbs free energy change of anatase is larger than that of amorphous flakes/films, the much lower γ of amorphous flakes/films makes their nucleation energy barrier lower than that of direct formation of anatase phase, rendering a preferable nucleation route toward unstable amorphous phase at the beginning. This numerical analysis, together with the experimental observation, evidence that the TiO₂ ALD growth at 600 °C follows the Ostwald–Lussac Law.

Regarding the TiO₂ NR morphology evolution, the initial study shows that NRs started to form after ~50 cycles of

growth. To further understand the anisotropic growth phenomenon that is responsible for NR formation, samples obtained from longer growth cycles were investigated. After 75 cycles of growth, HR HAADF STEM images revealed that the entire surface of single crystalline NR is covered with a ~2 nm thick percolated film (a mixture of polycrystalline TiO₂ with amorphous intercalation, Figure 3a). The atomic structure observed by the HR HAADF STEM is consistent with the anatase phase identified by XRD. The coexistence of amorphous and crystalline phases in the surface layer of TiO₂ NR represents a similar case as that observed from Si NW surface in the nucleation stage. This is thus considered as the secondary nucleation on the surface of evolved TiO₂ crystals, which still follows the Ostwald–Lussac Law. EELS line scans and mapping revealed a much lower Ti and O signal strength at the surface layer region compared to the NR body, indicating the crystalline layer is much less compact (Supporting Information Figure S8). From the 200-cycle sample, the base portion of the NR exhibited a clean and smooth surface; no percolated film or other defects were observed (Figure 3b-i). The percolated film started to appear at the middle region of the NR. It was a transient morphology with its thickness varying from a few angstroms (the bottom side) to ~1 nm (the top side) (Figure 3b-ii). Fully evolved percolated film was only found at the top portion of NR (Figure 3b-iii). EELS line scan demonstrated that the outmost tip of NR contained much less Ti and O, indicating this was the region under development, or actively growing (Figure 3b-iv). After 400 cycles (Figure 3c), the NR's body (i), side surface (ii), and front (iii, iv) all exhibited high-quality crystallinity and no percolated film could be observed (the amorphous layer observed in Figure 3c-iv is due to carbon deposition in STEM chamber).

The TiO₂ NR growth process can be observed more dynamically under TEM using electron beam illumination on a 75-cycle TiO₂ NR embryo (Supporting Information Figure S9). The electron beam may induce local heating due to the poor

thermal conductivity of the sample, or knockout damage that largely increases the mobility of individual atoms. Either effect would facilitate the recrystallization of TiO_2 and may recover the NR evolution process. TEM images along beam illumination show that the NR builds its body by sacrificing the surface percolated layers (evidenced by the shrinking of NR's diameter). This is because the surface crystallites are surrounded by amorphous films that are not epitaxially grown on the NR surface. When the mobility becomes high enough (e.g., under high temperature, 600 °C and hydroxyl group-rich environment), they could travel on the crystal surface and organize themselves to attach to appropriate NR surfaces following oriented attachment mechanism,^{23,36} as schematically shown in Figure 3d. Annealing a TiO_2 NR at 600 °C in the TEM chamber also provided supportive evidence to the oriented attachment-induced anisotropic NR growth (Supporting Information Figure S10). HRTEM images taken during the annealing process illustrate that at high temperature, the crystalline nanoparticle in the percolated film could align its crystal lattice with the NR lattice making the NR propagate along the (002) facet. Combining all above observations, we could suggest that the anisotropic growth is a result of shattering and migrating of percolated shells on manifold body and subsequent orientated attachment on high surface energy facet (the (002) facet of anatase TiO_2).^{37–39}

When the growth cycles approach 400, the density and surface area of NRs became much larger and the amount of precursor per unit area is much less than the early growth stages. Thus, once the value of $\ln S$ is lower than both the equilibrium products of amorphous particles and even amorphous film/flake, nucleation of amorphous particles and film/flakes is ceased. According to Figure 2e, if the activity product is higher than the equilibrium product of anatase at this time, nucleation and growth of anatase would proceed on the NR surface. This is the scenario we have observed at this stage. Two hundred cycles result is more or less an intermediate phase between early cycles and high cycles, where precursors with a mean-free-path of a few hundred nanometers may not reach the root region of NRs and the nucleation and growth of anatase dominates in this region. At the top rim of NR, larger $\ln S$ warrants the occurrence of nucleation and growth of amorphous phase.

The Ostwald–Lussac Law and orientated attachment observed in TiO_2 NR growth was further explored in ALD anatase TiO_2 films grown at 300 °C on ZnO NW sidewalls (Figure 4a). After five cycles of ALD growth, the NW's surface was covered with a discrete layer of amorphous TiO_x with the maximum thickness of 0.6 nm (Figure 4b). This corresponds to an averaged 0.06 nm per cycle, which is similar to low-temperature amorphous film growth rate.⁴⁰ After 10 cycles, a percolated film of crystalline TiO_2 nanoparticles with amorphous TiO_x film matrix appeared (Figure 4c). The TiO_2 nanoparticles did not exhibit any epitaxial relation with the ZnO lattice (inset of Figure 4c). The emergences of amorphous agglomerates and crystalline nanoparticles under 300 °C both occurred earlier than the 600 °C cases. Besides, diameter of the 10-cycle crystalline nanoparticles under 300 °C is ~ 2 nm, twice larger than the 10-cycle crystallites grown at 600 °C. This indicates that the nucleation stage proceeds faster at 300 °C than 600 °C. The faster rate makes the transient amorphous particles phase unobservable at 300 °C. In order to understand the accelerated nucleation rate at lower temperature, the nucleation induction time is considered, which is given by,³¹

$$t_{\text{ind}} = kc^{1-p} \propto J_n^{-1} \quad (3)$$

where k is a constant, p is the number of molecules in a critical nucleus and c is the precursor concentration. According to eq 3, c at 300 °C should be much higher than at 600 °C. One likely reason is that molecules' desorption probability decreases exponentially with the temperature, while other parameters are less temperature dependent.³¹ Therefore, at 300 °C the much lower desorption probability yields a significantly higher precursor molecule concentration on the surface, which renders a higher supersaturation ($\ln S$) as an activity product of precursor molecules and corresponding active surface dangling bonds and thus results in a shorter nucleation induction time.

After 35 cycles of ALD, crystalline nanoparticles grew larger; meanwhile the amorphous islands coalesced and became a continuous amorphous film (~ 2 nm, Figure 4d). This result indicates that both phase transition (from amorphous to crystalline TiO_2) and vapor deposition (propagation of amorphous layer) occurred simultaneously at 300 °C. As it proceeded to 50 cycles, the amorphous film reached ~ 5 nm with most crystalline nanoparticles buried inside (Figure 4e). Figure 4f shows a 100-cycle ALD result, where a percolated nanoparticle-amorphous thin film (~ 10 nm in thickness) was obtained. Compositions of both nanoparticle and film are confirmed to be TiO_2 by EELS. The 300 °C ALD process has two distinguishing differences compared to the 600 °C ALD: (1) the amorphous layer persists during the entire growth process; and (2) the small anatase nanoparticles do not agglomerate to form a NR embryo through the vapor-phase oriented attachment. The first difference is a direct outcome following the Ostwald–Lussac Law; while the second difference is governed by the oriented attachment principle. At 300 °C, coexistence of both amorphous and crystalline phases directly evidenced the operation of the Ostwald–Lussac Law. Whereas, the amorphous-to-crystalline ratio was much higher in the 300 °C products compared to the 600 °C products, indicating the phase transformation rate was much faster at 600 °C. This is consistent with the Ostwald–Lussac Law manifested in eq 1, in which the nucleation rate is strongly bounded to temperature. Oriented attachment requires that individual particles must have distinct facets, some of which have higher surface free energy in order to achieve anisotropic growth. Then self-organization proceeds by attaching neighboring crystalline nanoparticles onto high surface energy facets. At 300 °C, the diffusivity of amorphous TiO_x phase is much smaller than at 600 °C and therefore the formation of thermodynamically faceted particles become difficult, which disables the oriented attachment growth. In addition, mobility of crystalline particles has to be reasonable in order to enable orientation alignment and crystal attachment. Lower temperature (300 versus 600 °C) and the amorphous film coverage significantly restricted the mobility of the embedded nanoparticles. Last, lower temperature yielded a slower phase transition from amorphous film to crystalline particle and the accumulation of amorphous phase blocked the drifting of small particles for oriented attachment. This discovery suggests that the formation of a crystalline TiO_2 ALD film may be a result of the combination of layer-by-layer surface chemical absorption and subsequent phase transformation.

This research revealed the role of the Ostwald–Lussac law in high-temperature TiO_2 ALD growth processes. Atomic-resolution electron microscopy and elemental analysis manifest the evolution of TiO_2 nanostructures during ALD follows a

generic and explicit path from amorphous layers to amorphous particles to metastable crystallites and ultimately to stable crystalline forms. The evolution can be terminated at any intermediate stage yielding thin films or nanostructures with mixed phases. At high temperature, the amorphous–crystalline mixture can enable a unique anisotropic crystal growth behavior forming TiO₂ nanorods via the principle of vapor-phase oriented attachment. This discovery provides a new understanding of morphology and property variation and phase nonuniformity in ALD thin films and nanostructures. It suggests that in order to achieve desired morphology, phase, and property of ALD products surface chemistry should not be the only consideration. Emphasis should also be placed on phase diagrams of target materials and local kinetics.

■ ASSOCIATED CONTENT

Supporting Information

Supporting

Additional information and figures. This material is available free of charge via the Internet at <http://pubs.acs.org>.

■ AUTHOR INFORMATION

Corresponding Author

*E-mail: xudong@engr.wisc.edu.

Present Address

[†](J.S.) School of Engineering and Applied Sciences, Harvard University.

Notes

The authors declare no competing financial interest.

■ ACKNOWLEDGMENTS

The authors thank financial support from by U.S. Department of Energy, Office of Basic Energy Sciences under Award DE-SC0008711, and Air Force under Award FA9550-13-1-0168.

■ REFERENCES

- (1) George, S. M. Atomic Layer Deposition: An Overview. *Chem. Rev.* **2010**, *110*, 111–131.
- (2) Leskela, M.; Ritala, M. Atomic layer deposition (ALD): from precursors to thin film structures. *Thin Solid Films* **2002**, *409*, 138–146.
- (3) Niinisto, L.; Paivasaari, J.; Niinisto, J.; Putkonen, M.; Nieminen, M. Advanced electronic and optoelectronic materials by Atomic Layer Deposition: An overview with special emphasis on recent progress in processing of high-k dielectrics and other oxide materials. *Phys. Status Solidi A* **2004**, *201*, 1443–1452.
- (4) Wilk, G. D.; Wallace, R. M.; Anthony, J. M. High-kappa gate dielectrics: Current status and materials properties considerations. *J. Appl. Phys.* **2001**, *89*, 5243–5275.
- (5) Ando, T.; et al. Application of HfSiON to deep-trench capacitors of sub-45-nm-node embedded dynamic random-access memory. *Jpn. J. Appl. Phys., Part 1* **2006**, *45*, 3165–3169.
- (6) Huang, J. Y.; Wang, X. D.; Wang, Z. L. Controlled Replication of Butterfly Wings for Achieving Tunable Photonic Properties. *Nano Lett.* **2006**, *6*, 2325–2331.
- (7) Christensen, S. T.; et al. Supported Ru-Pt Bimetallic Nanoparticle Catalysts Prepared by Atomic Layer Deposition. *Nano Lett.* **2010**, *10*, 3047–3051.
- (8) Puurunen, R. L. Surface chemistry of atomic layer deposition: A case study for the trimethylaluminum/water process. *J. Appl. Phys.* **2005**, *97*, 121301.
- (9) Knez, M.; Niesch, K.; Niinisto, L. Synthesis and surface engineering of complex nanostructures by atomic layer deposition. *Adv. Mater.* **2007**, *19*, 3425–3438.

(10) Jur, J. S.; Parsons, G. N. Atomic Layer Deposition of Al₂O₃ and ZnO at Atmospheric Pressure in a Flow Tube Reactor. *ACS Appl. Mater. Interfaces* **2011**, *3*, 299–308.

(11) Takahashi, N.; Nonobe, S.; Nakamura, T. Growth of HfO₂ films using an alternate reaction of HfCl₄ and O₂ under atmospheric pressure. *J. Solid State Chem.* **2004**, *177*, 3944–3948.

(12) Brennan, T. P.; et al. Atomic Layer Deposition of CdS Quantum Dots for Solid-State Quantum Dot Sensitized Solar Cells. *Adv. Energy Mater.* **2011**, *1*, 1169–1175.

(13) Dasgupta, N. P.; et al. Atomic Layer Deposition of Lead Sulfide Quantum Dots on Nanowire Surfaces. *Nano Lett.* **2011**, *11*, 934–940.

(14) Shi, J. A.; Sun, C. L.; Starr, M. B.; Wang, X. D. Growth of Titanium Dioxide Nanorods in 3D-Confined Spaces. *Nano Lett.* **2011**, *11*, 624–631.

(15) Shi, J.; Hara, Y.; Sun, C. L.; Anderson, M. A.; Wang, X. D. Three-Dimensional High-Density Hierarchical Nanowire Architecture for High-Performance Photoelectrochemical Electrodes. *Nano Lett.* **2011**, *11*, 3413–3419.

(16) Yang, R. B.; et al. The Transition between Conformal Atomic Layer Epitaxy and Nanowire Growth. *J. Am. Chem. Soc.* **2010**, *132*, 7592.

(17) Ritala, M.; Leskela, M. Atomic layer epitaxy - a valuable tool for nanotechnology? *Nanotechnology* **1999**, *10*, 19–24.

(18) Ritala, M.; Leskela, M.; Nykanen, E.; Soininen, P.; Niinisto, L. Growth of Titanium-Dioxide Thin-Films by Atomic Layer Epitaxy. *Thin Solid Films* **1993**, *225*, 288–295.

(19) Liu, Y. Q.; Xu, M.; Heo, J.; Ye, P. D. D.; Gordon, R. G. Heteroepitaxy of single-crystal LaLuO₃ on GaAs(111)A by atomic layer deposition. *Appl. Phys. Lett.* **2010**, *97*, 162910.

(20) Ferguson, J. Biological Mineralization and Demineralization - Nancollas, G. *Miner. Mag.* **1983**, *47*, 421–421.

(21) Pellegrino, E. D. Biological Mineralization and Demineralization - Report of the Dahlem Workshop on Biological Mineralization and Demineralization, Berlin, October 18–23, 1981 - Nancollas, G. *Q. Rev. Biol.* **1983**, *58*, 611–611.

(22) Ostwald, W. Studien über die Bildung und Umwandlung fester Körper. *Z. Phys. Chem* **1897**, *22*, 289–330.

(23) Penn, R. L.; Banfield, J. F. Imperfect oriented attachment: Dislocation generation in defect-free nanocrystals. *Science* **1998**, *281*, 969–971.

(24) Penn, R. L.; Banfield, J. F. Oriented attachment and growth, twinning, polytypism, and formation of metastable phases: Insights from nanocrystalline TiO₂. *Am. Mineral.* **1998**, *83*, 1077–1082.

(25) Miiikkulainen, V.; Leskela, M.; Ritala, M.; Puurunen, R. L. Crystallinity of inorganic films grown by atomic layer deposition: Overview and general trends. *J. Appl. Phys.* **2013**, *113*, 021301.

(26) Brydson, R.; et al. Electron Energy-Loss Spectroscopy (EELS) and the Electronic-Structure of Titanium-Dioxide. *Solid State Commun.* **1987**, *64*, 609–612.

(27) Ranade, M. R.; et al. Energetics of nanocrystalline TiO₂. *Proc. Natl. Acad. Sci. U.S.A.* **2002**, *99*, 6476–6481.

(28) Barin, I.; Knacke, O. *Thermochemical Properties of Inorganic Substances*; Springer-Verlag: New York, 1973.

(29) Yau, S. T.; Petsev, D. N.; Thomas, B. R.; Vekilov, P. G. Molecular-level thermodynamic and kinetic parameters for the self-assembly of apoferritin molecules into crystals. *J. Mol. Biol.* **2000**, *303*, 667–678.

(30) Yau, S. T.; Vekilov, P. G. Quasi-planar nucleus structure in apoferritin crystallization. *Nature* **2000**, *406*, 494–497.

(31) De Yoreo, J. J.; Vekilov, P. G. Principles of crystal nucleation and growth. *Biomaterialization* **2003**, *54*, 57–93.

(32) Wang, X.; Shi, J. Evolution of titanium dioxide one-dimensional nanostructures from surface-reaction-limited pulsed chemical vapor deposition. *J. Mater. Res.* **2013**, *28*, 270–279.

(33) Yau, S. T.; Vekilov, P. G. Direct Observation of Nucleus Structure and Nucleation Pathways in Apoferritin Crystallization. *J. Am. Chem. Soc.* **2001**, *123*, 1080–1089.

- (34) Zhang, H. Z.; Banfield, J. F. Kinetics of Crystallization and Crystal Growth of Nanocrystalline Anatase in Nanometer-Sized Amorphous Titania. *Chem. Mater.* **2002**, *14*, 4145–4154.
- (35) Zhang, H. Z.; Banfield, J. F. Understanding Polymorphic Phase Transformation Behavior during Growth of Nanocrystalline Aggregates: Insights from TiO₂. *J. Phys. Chem. B* **2000**, *104*, 3481–3487.
- (36) Lovley, D. R. Geomicrobiology: Interactions between microbes and minerals. *Science* **1998**, *280*, 54–55.
- (37) Oskam, G.; Nellore, A.; Penn, R. L.; Searson, P. C. The Growth Kinetics of TiO₂ Nanoparticles from Titanium(IV) Alkoxide at High Water/Titanium Ratio. *J. Phys. Chem. B* **2003**, *107*, 1734–1738.
- (38) Barnard, A. S.; Zapol, P.; Curtiss, L. A. Modeling the morphology and phase stability of TiO₂ nanocrystals in water. *J. Chem. Theory Comput.* **2005**, *1*, 107–116.
- (39) Diebold, U.; Ruzycski, N.; Herman, G. S.; Selloni, A. One step towards bridging the materials gap: surface studies of TiO₂ anatase. *Catal. Today* **2003**, *85*, 93–100.
- (40) Wilson, C. A.; Grubbs, R. K.; George, S. M. Nucleation and Growth during Al₂O₃ Atomic Layer Deposition on Polymers. *Chem. Mater.* **2005**, *17*, 5625–5634.